JOURNAL OF AIRCRAFT
Vol. 47, No. 3, May–June 2010

Roll Control via Active Flow Control: From Concept to Flight

A. Seifert,* S. David,* I. Fono,* O. Stalnov,* and I. Dayan*
Tel-Aviv University, 69978 Tel-Aviv, Israel

DOI: 10.2514/1.45910

This paper describes a series of experiments that enabled a flight demonstration of roll control without moving control surfaces. That goal was achieved using a wing with a partial span Glauert-type airfoil, characterized by an upper-surface boundary-layer separation from the two-thirds chord location at all incidence angles. The flow over that region was proportionally controlled using zero-mass-flux unsteady excitation emanating from piezofluidic actuators. The control was applied to one wing at a time, resulting in gradual suppression of the boundary-layer separation, increased lift, and reduced drag, leading to a coordinated turning motion of the small electric drone. The extensive multidisciplinary study (starting from the actuator adaptation, the airfoil integration, and the two-dimensional wind-tunnel tests) led to the selection of a configuration for the flight demonstrator. Further development of a lightweight wing and piezofluidic actuators, along with a compact, lightweight, energy-efficient electronic drive system, was followed by full-scale wind-tunnel tests and three successful flight tests. It was flight-demonstrated that active flow control can induce roll moments that are sufficient to control the vehicle flight path during cruise, as well as during landing. A linear model was used to predict the roll motion of the active-flow-controlled drone, with reasonable agreement to the flight-test data. The current study resulted in several pioneering (to the best of our knowledge) achievements that should pave the way to further integration of active-flow-control methods in flight vehicles for hingeless flight attitude and flight-path control, as well as improved performance and increased reliability with lower observability.

Nomenclature

b	=	wingspan, m
C_D	=	three-dimensional drag coefficient $D/(\rho V^2 s/2)$
$C_{D_{\text{Betz}}}$	=	two-dimensional drag coefficient corrected according to Betz [1]
C_L	=	three-dimensional lift coefficient $L/(\rho V^2 s/2)$
C_l	=	two-dimensional lift coefficient $l/(\rho V^2 s/2)$
C_{l_p}	=	damping in roll $\partial C_R/[\partial(pb/2V)]$
C_{l_r}	=	rolling moment due to yawing velocity $\partial C_R/[\partial(rb/2V)]$
C_{l_β}	=	rolling moment due to sideslip angle $\partial C_R/\partial\beta$
C_n	=	yaw moment coefficient $N/(\rho V^2 sb/2)$
C_{n_p}	=	yawing moment due to rolling velocity $\partial C_n/[\partial(pb/2V)]$
C_{n_r}	=	damping in yaw $\partial C_n/[\partial(rb/2V)]$
C_{n_β}	=	yawing moment due to sideslip angle $\partial C_n/\partial\beta$
C_R	=	roll moment coefficient $R/(\rho V^2 sb/2)$
C_y	=	side-force coefficient $F_y/(\rho V^2 s/2)$
C_{y_β}	=	side force due to sideslip angle $\partial C_y/\partial\beta$
C_μ	=	excitation momentum coefficient hU_p^2/cV^2
c	=	wing chord, m
D	=	drag force, N
F_y	=	side force, N
h	=	width of actuators exit slot, m
I_x, I_z	=	moments of inertia about the roll and yaw axis, respectively, kg · m^2
L	=	three-dimensional lift force, N
l	=	two-dimensional lift force, N
m	=	mass of the airplane, kg
p, r	=	angular velocities about the roll and yaw axis, respectively, deg /s
q	=	dynamic pressure $\rho V^2 s/2$, Pa
R, N	=	moments about the roll and yaw axis, respectively, N · m
s	=	wing area, m^2
U_p	=	peak excitation velocity at the actuators exit slot, m/s
V	=	measured indicated air speed, m/s
α	=	angle of attack, deg
β	=	sideslip angle, deg
δ_a	=	aileron deflection angle, deg
ϕ	=	roll angle, deg
ψ	=	yaw angle, deg

I. Introduction

ACTIVE flow control (AFC) of boundary-layer separation has been intensively studied at Tel-Aviv University (TAU) and elsewhere for close to three decades [2]. The delay of boundary-layer separation is a high-risk high-payoff task, with studies that date back to Prandtl [3], who formulated the boundary-layer equations and identified their failure due to boundary-layer detachment. Prandtl also suggested a remedy: using steady suction and cylinder rotation to replace and/or reenergize the sluggish boundary-layer flow. Steady suction and wall tangential blowing [4] were intensively studied and even reached production airplanes, but they were abandoned due to low efficiency, excessive weight, complexity, and reliability concerns. Unsteady control of shear layers has the potential of overcoming the efficiency barrier, provided that flow instability (rather than brute force) is applied. Oster and Wygnanski [5] provided a benchmark demonstration of forced excitation of turbulent shear layers for mixing enhancement. Enhanced mixing is the leading mechanism explaining the efficacy of AFC for boundary-layer control (BLC) over aerodynamic surfaces. Early studies of active BLC focused on enhancing the lifting performance of rather benign airfoils, such as the NACA 0012 and 0015 at low Reynolds numbers (below one million). Many published studies suffered from the complex interplay between the transition promotion of laminar boundary layers (resulting in postponed separation) and the delay of turbulent boundary-layer separation due to energized near-wall flow. The study of Seifert and Pack [6] provided the first demonstration of active BLC at a Reynolds number of up to 30 million, corresponding to transport planes at takeoff. However, more recently, it became apparent that active BLC can not increase the maximum lifting performance of well-designed airfoils operating at their design point,

Received 9 June 2009; revision received 3 September 2009; accepted for publication 24 September 2009.

*Faculty, School of Mechanical Engineering.

at least until an engineering design tool that includes AFC becomes available [7]. This is because AFC was considered a retrofit rather than an integrated design capability in all known studies. Until such a design capability is available, the AFC technology could bring significant benefits in several other focal areas. The following are possible benefits:

1. Maintenance of high lift at low Reynolds numbers (below 100,000), for which the natural transition is absent.

2. Management of laminar and, more important, turbulent separated flows (bubbles or burst vortices over delta wings).

3. Reattachment of separated flows for generating control moments [8–10].

4. Drag reduction of bluff bodies (open-loop studies [11,12]).

The above applications are essentially the manifestations of the same mechanism, AFC, applied over different geometries at different flow conditions to mitigate boundary-layer separation.

The current study falls into the third category. By partially or fully reattaching the separated flow at the aft upper region of a modified Glauert-type airfoil [10,13–15], it is possible to significantly increase the lift and significantly reduce the drag over the entire relevant angle-of-attack range. Our concept is inherently different from other studies applying AFC to conventional airfoils (limited to poststall or requiring intentional separation of the flow over sections of the airfoil). The current separation control approach could be achieved in a gradual manner, proportional to the magnitude of the control authority. By applying the AFC over segments of a finite-span wing, it should be possible to generate sufficient roll moments to control the roll axis and roll motions of an airplane while reducing the drag on the higher lift wing, resulting in proverse yaw. This is what the current study was aimed to achieve and demonstrate in flight.

II. Description of Research Tasks

A series of design and experimental tasks were performed at the following locations:

1. The actuator calibration lab at TAU was used for calibrating the actuator prototype, the actuators for the two-dimensional (2-D) tests, and the actuators used for flight tests with the ground-drive electronics, as well as with the custom-made lightweight flight-drive electronics.

2. The Meadow–Knapp low-speed wind tunnel (LSWT) at TAU was used for the 2-D airfoil tests. Lift, moment, and form drag were calculated from surface pressures, and drag was calculated by wake integration. A 21% thick 275 mm chord airfoil with a modified Glauert-type airfoil (used previously by Seifert and Pack [15] and by Yom-Tov and Seifert [10], but cropped at $0.95c$) with a piezofluidic actuator array located at 67% of the chord, which was fabricated from fiberglass epoxy skin and actuators made from aluminum, was integrated in it.

3. Vehicle and wing design were done by the Israel Aerospace Industries (IAI) engineering center staff. To save resources, an existing small electric drone was used. The wing was redesigned to allow increased airplane weight and lower stall speed, and the body was extended to allow storage of the actuators' drive electronics and integration with the vehicle control system.

4. The LSWT at IAI was used to test the complete airplane just before flight tests. Baseline aerodynamic data, as well as AFC data, using both a lab electronic drive system and the flight-drive system with its remote control (R/C) capabilities, were tested. These experiments were crucial for reducing the risks of the first flight test.

5. Three successful flight tests were conducted, including data acquisition from the drone telemetry system that was later used to validate three-degree-of-freedom (3-DOF) flight simulator data.

The following subsections of the paper describe each of these defined tasks.

A. Adaptation and Testing of Lightweight Actuators and Flight-Drive System

The chord of the modified Glauert airfoil for the flight tests was 275 mm (similar to the existing drone wing chord). Its maximum thickness was 21%, which resulted from cropping the last 5% of the previously used modified Glauert airfoil. Significant internal wing volume became available for instrumentation. This was accompanied, however, by strict requirements for light weight and energy efficiency. The technology selected for actuation was piezoelectric, due to its compactness, low weight, and superior energy efficiency when compared with other known actuation concepts (see Arwatz et al. [16] for a discussion on the subject). The TAU-made piezofluidic actuators were proven to be very compact and robust [17]. The actuators consume about 1 to 3 W while operating at the Helmholtz resonance frequency and generating peak exit velocities in the order of 50 m/s from a 1-mm-wide 40-mm-long slot. Figure 1 shows a cross section of the Glauert airfoil with the actuators installed. The total length of the actuator is less than 50 mm, and its thickness is less than 7 mm. During the first-generation 2-D tests, the actuators were installed from the side and bolted to the fiberglass skin from the outside. This was altered so that the actuators were installed and bolted from the outside for the flight-test wing (see Fig. 2), due to the one-block structure of the wing. Each actuator was instrumented with two piezoelectric disks and had its own sealed cavity, open only to the external upper surface through the exit slot. Figure 1 shows that the slot ejected the zero mass flux (ZMF) excitation in a shallow downstream-directed angle, as in all the previous studies on this type of geometry. The free end of the actuator was supported by the main beam of the wing.

The prototype actuator (made by the rapid prototyping technique) was bench-top tested for frequency and peak exit velocity by placing a calibrated hot wire (uncertainty of 2%) and measuring the peak exit slot velocity. The Helmholtz resonance frequency was found to be about 1200 Hz. An amplitude scan of the prototype actuator is shown in Fig. 3a. The peak velocity curve (left side ordinate) shows the typical linear, and then quadratic, behavior of the peak velocity versus the excitation voltage, with the target of $U_p = 40$ m/s reached at about 100 V alternating current (AC), or VAC. The right-side ordinate, showing the power consumed by the actuator, indicates that about 3 W are required for each actuator to generate the maximum desired fluidic excitation. This should bring the total power required for roll control close to 40 W. The weight of the prototype actuator unit was less than 30 g.

The performance of the actuator prototype was deemed sufficient to freeze the design and proceed to integrating this design in the wing. For ease of assembly and integration, it was decided to fabricate the actuators from aluminum for subsequent wind-tunnel and flight tests.

In laboratory experiments, the weight and power consumption of the drive electronics to operate the actuators are insignificant. However, it is crucial to minimize weight and power consumption of the flight actuator drive system. In addition, the drive system should be integrated with the drone R/C system and be immune to electromagnetic noise. Also, the system should not adversely affect

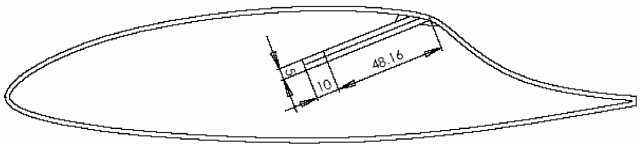

Fig. 1 A cross section of the modified Glauert airfoil. Chord is $c = 275$ mm, and thickness is 21%. The actuators' exit slot is located at $x/c = 0.67$, ejecting the ZMF excitation in a shallow downstream-directed angle.

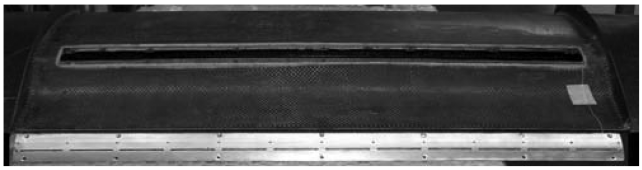

Fig. 2 A rear view of the airplane wing, the opening for the actuators, and the actuators' exit slots before being installed in the wing. An array of 12 actuators was installed in each wing.

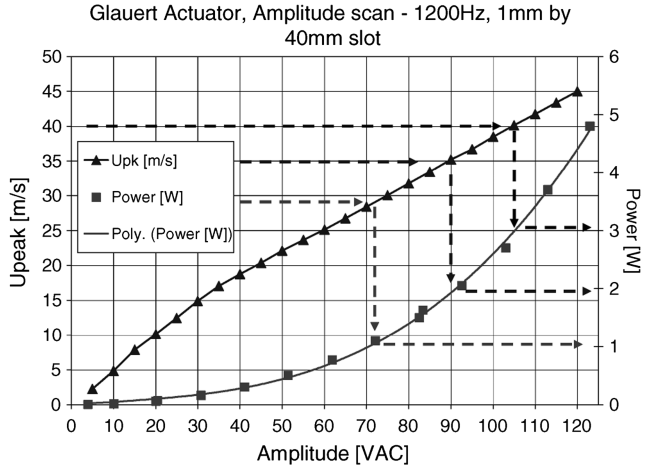

a)

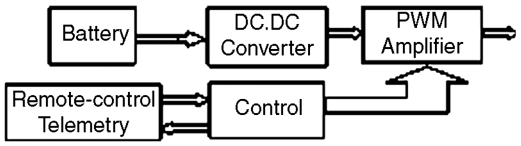

b)

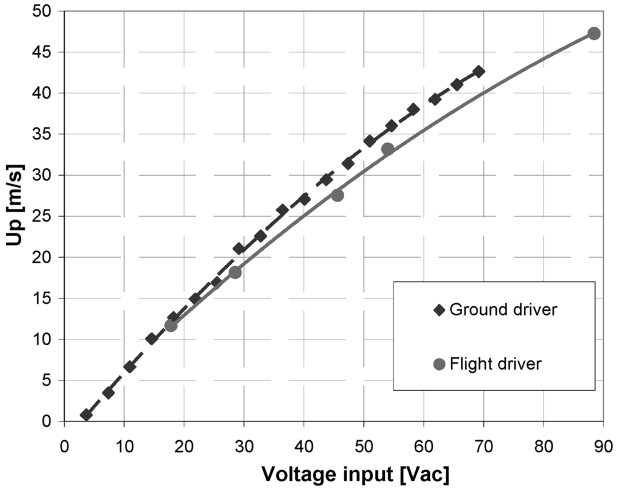

c)

Fig. 3 Details of the prototype actuators: a) amplitude response test of the prototype actuator at the Helmholtz frequency, operated by the ground-drive system (the left-side ordinate shows the peak slot exit velocity and the right-side ordinate shows power consumption, both plotted against the input AC voltage); b) block diagram of the flight actuator drive system; and c) amplitude response of the airfoil actuators at 1380 Hz, driven by the ground system (blue diamonds) and by the prototype of the flight-drive system (circles). Attaining approximately $U_p = 40$ m/s consumed only about 2 W per actuator for the airfoil and wing actuators.

the other components of the drone. Furthermore, it should be robust enough to withstand vibrations and landing impact.

Figure 3b shows the block diagram of the flight electronic drive system designed to operate the actuators in flight; it is operated via the R/C. The response of the actuators' output was intended to be proportional to the stick deflection, mimicking regular aileron operation. The flight electronic drive system was connected to the R/C receiver as a standard servo channel. In AFC flight mode, the stick deflection was transmitted by the servo channel and, in turn, it modulated the pulse width of a resonant direct current (DC)-to-AC converter [DC–DC converter with a pulse-width modulation (PWM) amplifier]. The output of the amplifier was bandpass-filtered with an inductor–capacitor resonator; thus, the voltage applied to the actuators was a sine waveform at the actuator's Helmholtz resonance frequency (1400 Hz, increased from the approximate 1200 Hz of the resin-made actuator prototype), and the amplitude of the excitation signal was proportional to the stick deflection (in the range of 30 to 110 VAC). This voltage range was selected based on the aerodynamic response to actuation, as shown in Sec. II.B. The excitation voltage was switched to the left- or right-wing actuators according to the direction of the desired roll. The flight-drive system was powered by the airplane's main battery at a nominal 16 V of DC. Because of the high efficiencies of the DC–DC converter and the PWM amplifier, the overall power efficiency achieved was close to 90%. The dimensions of the flight electronic drive system are 8 by 10 by 24 cm, and it weighs about 800 g.

B. Two-Dimensional Airfoil Experiments at Tel-Aviv University

After the layout and design of the lightweight actuators were validated to provide the target performances during the bench-top tests, the airfoil for the 2-D wind-tunnel tests and the 12-actuator

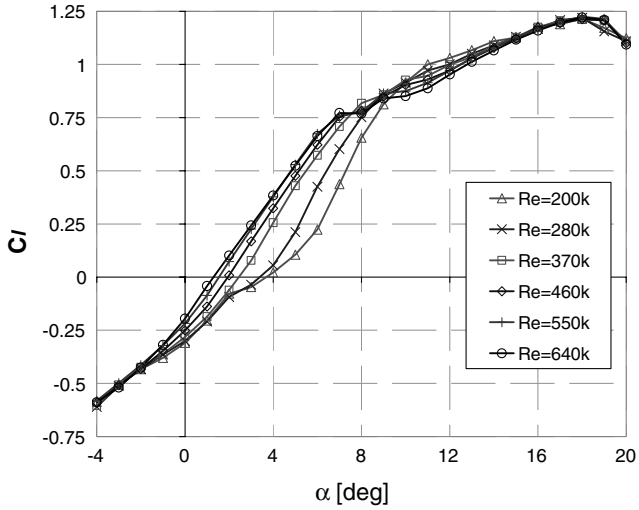

Fig. 4 Reynolds number effect on the lift of the clean modified Glauert airfoil performance 2-D TAU test.

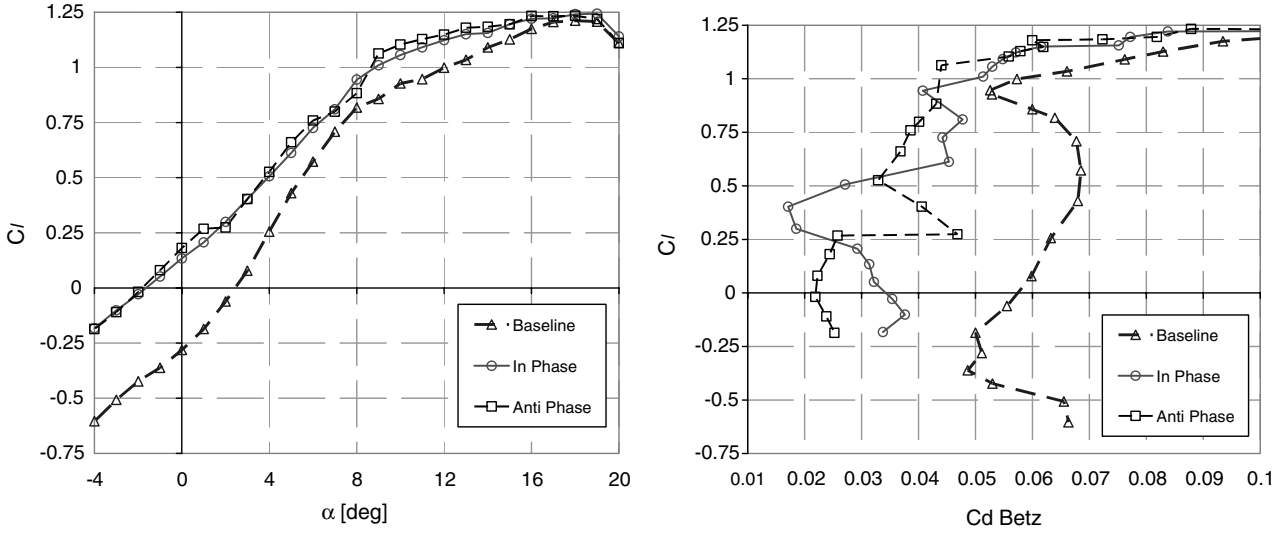

a) b)

Fig. 5 The effect of actuation on a) the lift vs incidence and b) on the airfoil lift vs drag. $Re = 370$ k and $U_p = 40$ m/s, forcing all actuators in phase and every other actuator phase inverted (termed antiphase). Triangles denote baseline.

array was designed and fabricated. The airfoil was constructed from a 2-mm-thick fiberglass epoxy skin. Its chord was 275 mm, and its span was equal to the tunnel's width, 609 mm. The model was instrumented with 31 pressure taps along its centerline and two additional rows of spanwise pressure taps, located at $x/c = 0.1446$ and 0.8. The 12-actuator array was fabricated from aluminum, instrumented, bench-top tested, and installed in the airfoil. The performance of the actuators made from aluminum exceeded those of the rapid prototype actuator, due to higher rigidity and tighter tolerances. The enhanced rigidity of the aluminum actuator resulted in an increase of the Helmholtz resonance frequency from 1200 to 1400 Hz.

The performance of the actuators with the ground and flight-drive electronics was tested and found to be identical, shown by the amplitude scan of the peak excitation magnitude, presented in Fig. 3c.

After the actuator fabrication and bench-top testing, the airfoil was instrumented and installed in the 1.5-m-high 0.609-m-wide test section of the Meadow–Knapp LSWT at TAU. First, the baseline performances of the 21%-thick Glauert airfoil were tested, at the Reynolds number range intended for the flight tests (Re= 280, 000–460, 000), with additional lower and higher Reynolds numbers for completeness. The lift performances of the 2-D modified Glauert airfoil are presented in Fig. 4.

Because of the massive flow separation from the aft upper surface of the airfoil (Fig. 1), at all incidence angles, and the complex interplay between the laminar-turbulent transition and the boundary-layer separation on such an airfoil at low Reynolds numbers, the baseline clean airfoil lift slope changes significantly at low incidence. As the Reynolds number increases, the lift slope becomes constant, and the lift at low incidence increases. The maximum lift of the baseline clean airfoil is about 1.25, and the stall incidence is 18 deg.

Following the studies of Seifert and Pack [15] and Yom-Tov and Seifert [10], it was expected that significant lift increment would be obtained at low and medium incidence angles when partial or complete flow reattachment would be affected by the fluidic excitation, applied at $x/c = 0.67$. Indeed, when the actuators were operated either in a unison-phase or a π-phase shift between every actuator pair (Fig. 5a), a significant lift increment was attained. Note that, at this excitation magnitude, the unison-phase actuation results in a smoother lift curve than the antiphase (π) distribution, whereas the latter provides a somewhat larger lift increment, as was previously noted by Seifert et al. [18] and Timor et al. [9].

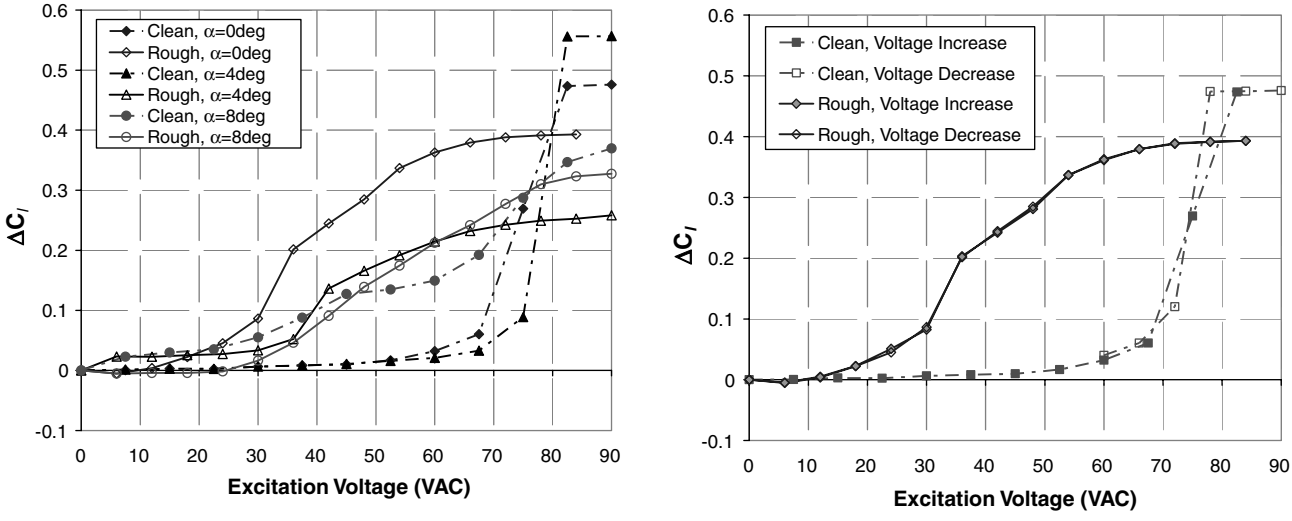

a) b)

Fig. 6 Lift increment data vs the excitation magnitude with uniform phase at $Re = 280, 000$: a) three angles of attack, smooth airfoil data (filled symbols), and rough airfoil data (empty symbols) (data taken when voltage increases continuously) and at b) $\alpha = 0$ deg, showing lack of hysteresis, rough airfoil, voltage increasing data (filled symbols), and voltage decreasing data (empty symbols).

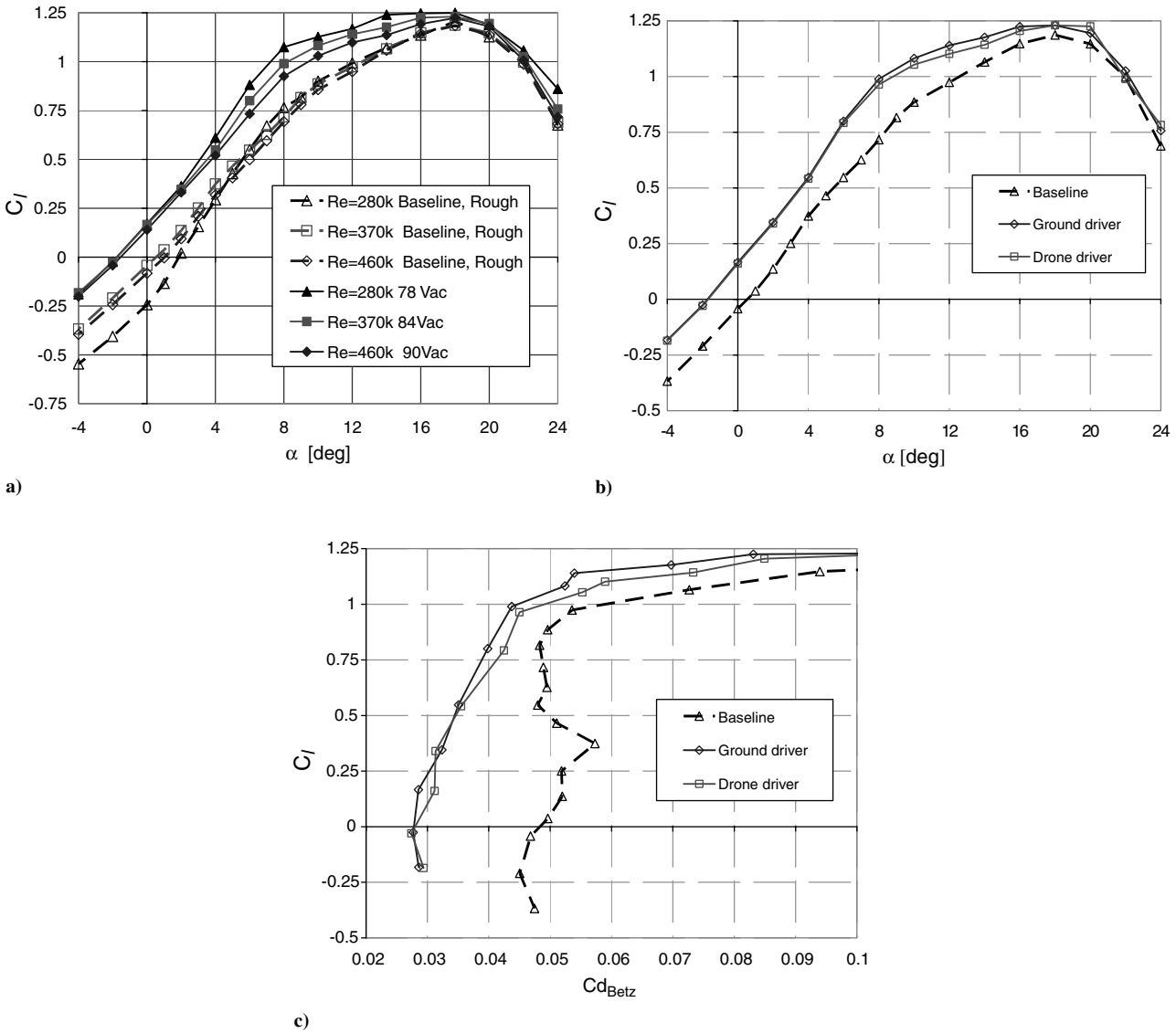

Fig. 7 Excitation effects on lift and drag: a) the lift performance of the baseline and controlled Glauert airfoil at the target Reynolds number range (tripped boundary layer); b) the baseline and controlled lift vs incidence at $Re = 370,000$, operated by the ground- and flight-drive systems (all actuators operate in unison, 85 VAC, $U_p \sim 45$ m/s); and c) the baseline and controlled lift vs drag at $Re = 370,000$, operated by the ground- and flight-drive systems (85 VAC, $U_p \sim 45$ m/s).

A concomitant drag reduction is associated with the actuation, the separation control, and the lift increment, as shown in Fig. 5b. The drag is, essentially, halved by the actuation. This is a desirable feature for roll control, because natural trimming will take place. When the lift increases on the controlled wing (or part of), the drag decreases, so that the nose turns into the flight path induced by the roll. On the other hand, undesirable and complex drag variations can be noted at low incidence; these, however, disappear at higher excitation magnitudes and tripped boundary-layer conditions, as will later be shown.

These complex phenomena are accentuated when one considers the lift response to alternation of the excitation magnitude. The results, shown in Fig. 6a, present an almost-step response (steady state) of the lift increment to increasing the excitation magnitude. This response is highly undesirable, because we are interested in a gradual aerodynamic response. It was again suspected that this response was due to the interplay between the natural boundary-layer laminar-turbulent transition, the boundary-layer separation, and its control. It was found that, at higher incidence (Fig. 6a, $\alpha = 8$ deg) and higher Reynolds numbers (not shown), the amplitude response of the lift is more gradual. This led us to force transition upstream of the actuation location, achieved by placing grit no. 60 on a 12-mm-wide double-sided tape (of thickness less than 0.1 mm) at $x/c = 0.4$. Indeed, the response of the rough airfoil to the increase in the excitation magnitude became significantly more gradual (Fig. 6a), although the maximum lift increment was reduced. This is expected, because the forced transition just upstream of the laminar separation (in natural flow conditions) delays the boundary-layer separation. However, the fact that the excitation is still effective and increases lift indicates that separation downstream of the actuator was not completely eliminated. The remaining potential lift increment of 0.2 to 0.35 was deemed sufficient for the purpose of the present study. Because the response to excitation magnitudes lower than 30 VAC was very weak, it was decided to set any deviation from a neutral AFC aileron setting (on the R/C stick) to 30 VAC. Figure 6b indicates the lack of hysteresis effect due to variations of the excitation magnitude.

Figure 7a presents the baseline and controlled rough Glauert airfoil lift versus the airfoil incidence angle. The high sensitivity of the baseline to the Reynolds number (compare to Fig. 4) is significantly reduced. A significant, though not constant, lift increment is available at all relevant incidence angles, with AFC activated. Note the different excitation magnitudes at the three Reynolds numbers, resulting in excitation momentum coefficients (C_μ) of 0.04, 0.025, and 0.018 at $Re = 280,000$, 370,000, and 460,000, respectively. The slot width is $h = 1$ mm, and the chord is $c = 275$ mm. The data also indicate a small lift increment, even at the stall angle. The reduction of the Reynolds number sensitivity and the attainment of the gradual lift

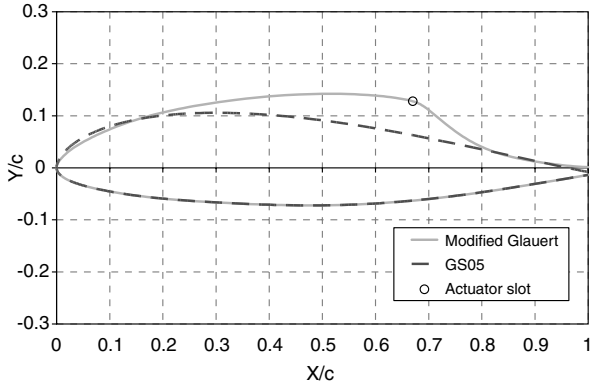

Fig. 8 The Glauert and the conventional airfoil contours (used for the central region of the wing and for the wing tips) with a common lower surface. The circle on the Glauert airfoil contour indicates the actuator slot location.

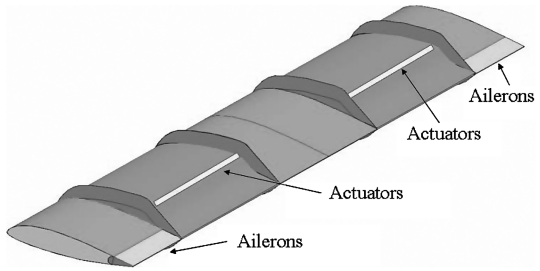

Fig. 11 The layout of the wing. The sections marked as actuators are the Glauert AFC sections, and the other sections are the conventional airfoils. The conventional ailerons are also shown at both wing tips. The middle and Glauert sections are 600 mm each. The aileron sections are 300 mm each. The aileron is 20% of the chord. A switch on the R/C was used to alter the joystick purpose, from controlling the aileron deflection to controlling the AFC voltage to either the right or left wings.

increment at all incidence angles, due to the actuation, enabled us to proceed to the design of the wing and the entire airplane for the full-scale wind-tunnel tests and for the flight tests.

The lift data shown in Fig. 7b present the baseline and controlled 2-D Glauert airfoil performances, as measured at TAU. The controlled data were acquired when the ground or the flight electric drive system operated the piezoactuators array. All actuators were operated in unison, in order to simplify the electric drive system, although it was found that operation in antiphase was more effective, as well as significantly less noisy due to destructive interference. Note that the results of the actuation are identical, regardless of the ground or the flight excitation electronics. At this Reynolds number (the core of the velocity range of the planned flight tests) and with the grit-tape roughness strip applied, an almost-uniform-lift increment of about 0.2–0.3 is attained at incidence angles from −4 to 12 deg, and a smaller lift increment was attained, even at a poststall incidence of 20 deg. This is a highly desirable trend.

Figure 7c shows the lift–drag polar of the 2-D Glauert airfoil at the TAU tunnel, for the baseline and the two actuation drive electronics. Again, the results of the flight-drive electronics are indistinguishable from the ground-drive electronics. Note that the minimum drag is reduced from about 0.05 to about 0.03 with effective actuation, and, even at a lift coefficient of 0.75 to 1, there is a 20% drag reduction. Further reduction is possible with alternating phase operation, requiring only minor additional development of the drive system.

Note that the complexity of the drag behavior of the smooth 2-D Glauert airfoil, identified in Fig. 5b, disappears with forced transition applied upstream of the actuation location, shown in Fig. 7c.

Fig. 9 A rear view of the Glauert section of the wing with the actuator exit slots. Each slot is 40 by 1 mm, with 5 mm of separation between each actuator pair. A 12-actuator array was installed in each wing.

C. Vehicle and Wing Design

The vehicle used for the flight tests was a modification of an existing IAI platform. It is an electric-powered vehicle with an original maximum weight of 5 kg and a speed range of 20–40 m/s. It can fly for about 1.5 h. In the current project, the maximum weight was increased to about 7.5 kg, and the stall speed was reduced to about 15 m/s for low-speed AFC testing. The new vehicle wing span was elongated to 2.4 m (from the original 1.8 m span), whereas the chord was unchanged at $c = 0.275$ m. The wing comprises two different airfoils, for safety and enhanced lift. Figure 8 shows a comparison of the modified Glauert airfoil and the conventional airfoil contours used. The conventional airfoil was designed with a lower surface contour, similar to that of the Glauert airfoil, but with a thickness ratio of 17.3%. Its maximum lift was computed to be about 0.15 higher than that of the modified Glauert airfoil, whereas its drag

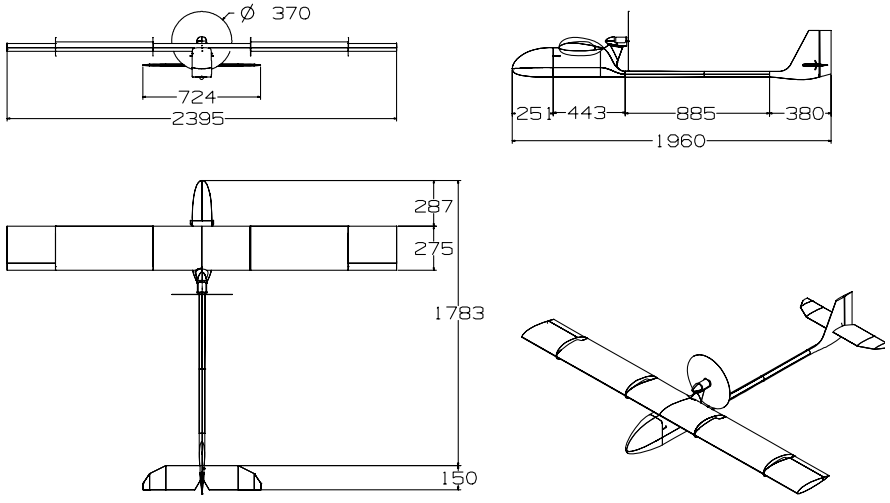

Fig. 10 The configuration of the flight demonstrator. Dimensions are in mm. Wing surface is 0.66 m^2 and wing incidence is 3 deg at airplane zero incidence.

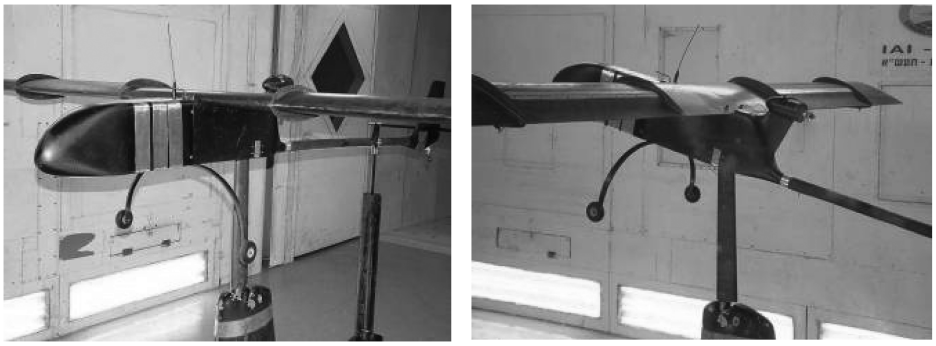

a) b)

Fig. 12 The airplane as installed at IAI LSWT: a) front view and b) rear view.

was predicted to be much lower, about 0.0150, at conditions of $C_l = 0.8$, a Reynolds number of 300,000, and a natural laminar case.

Figure 9 shows a rear view of the Glauert section of the wing, with the exit slots of the piezofluidic actuator array shown. To eliminate premature flow separations, the assembly of the wing assured smooth transition between the fiberglass and the aluminum parts.

Figures 10 and 11 show the layout of the wing and the drone, respectively. The 30 cm sections inboard from each wing tip are equipped with conventional ailerons. The next 60 cm of each wing are composed of the modified Glauert airfoil and equipped with an array of 12 actuators each. The 60 cm central section of the wing is of conventional airfoil and used to connect the wing to the body.

Figure 10 presents the layout of the airplane, with the AFC wing shown in Fig. 11. The central part of the body was elongated by 20 cm (as seen in Fig. 12a) to accommodate additional equipment, such as the actuation drive electronics. The tail boom was elongated to increase the pitching moment of the tail and the lateral stability. Details of the wing design are seen in Fig. 11. End plates were positioned between the Glauert and the conventional airfoil sections, because the geometries of the upper surfaces of the two airfoils are not identical (Fig. 8), in order to reduce three-dimensional (3-D) effects. Smooth fairing between the two sections was considered but not implemented (at present) to save costs.

The total weight of the actuation system was about 1800 g, of which 500 g was the weight of each set of 12 actuators. The maximum power consumption of one actuator array (set of 12) was 45 W, including the drive electronics. With some additional refinements, the total weight of the actuators and the flight-drive system could be reduced by at least 50%.

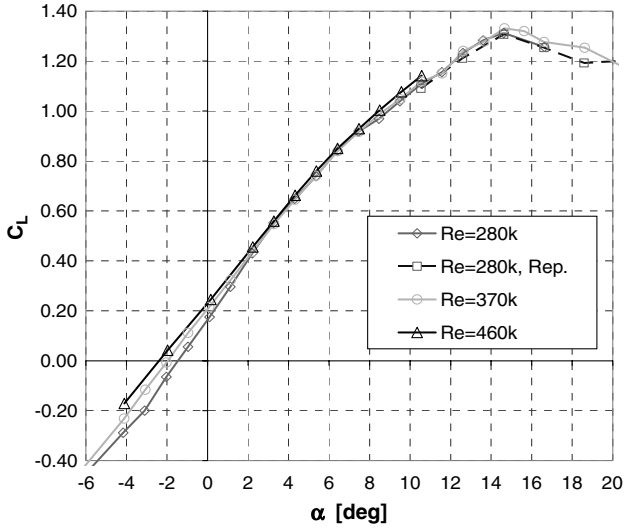

Fig. 13 The baseline lift of the plane, as measured at IAI LSWT, at the Reynolds number range corresponding to 15, 20, and 25 m/s. Roughness strip applied.

D. Vehicle Low-Speed Wind-Tunnel Tests

Full-scale experiments at the planned-flight Reynolds number range were performed on the flight-ready drone during a short entry (1.5 days) to the IAI LSWT. The test-section dimensions are 2.4 m high and 3.6 m wide. The velocity range is 10 to 100 m/s. The model was mounted on a central bayonet and an aft alpha rod. No image tests were performed. Figures 12a and 12b show photos of the drone installed in the test section of the IAI LSWT. The model was powered, and some power runs were also performed to validate that sufficient thrust was available. When the motor was not operated, the pusher propeller was removed.

Figure 13 shows the lifting performance of the plane in the wind tunnel at a freestream velocity of 20 m/s. The maximum lift coefficient was found to be about 1.3 at about 15 deg, as expected from the 2-D Glauert airfoil tests and the calculations of the conventional airfoil, considering the 3 deg wing incidence at the 0 deg airplane incidence. An operationally desirable mild stall was measured. Note that the lift slope of the blended airfoils wing is almost constant in the range $-2 \text{ deg} < \alpha < 3$ deg, a good trend when compared with that of the 2-D Glauert airfoil lift curve (Fig. 7b). However, the lift slope is significantly reduced for $\alpha > 6$ deg, as it is for $\alpha < 9$ deg for the Glauert-type airfoil (Fig. 7b). These results are consistent with the 3 deg wing setting at airplane zero incidence.

Figure 14 shows the lift–drag polar of the airplane at a speed of 20 m/s, corresponding to the main Reynolds number of 370,000. The minimum uncontrolled drag of the airplane is about 0.08, attributed to the body, the engine nacelle, the landing gear, and the relatively high drag of the uncontrolled separations on the Glauert airfoil sections of the wing (about 0.05, as shown in Fig. 7c, for half the span of the wing). Operating only one wing actuator increased the lift by about 0.1 and reduced the drag by 0.005 to 0.01 over most of the lift range. This would indicate a lift increment of about 0.3 and a

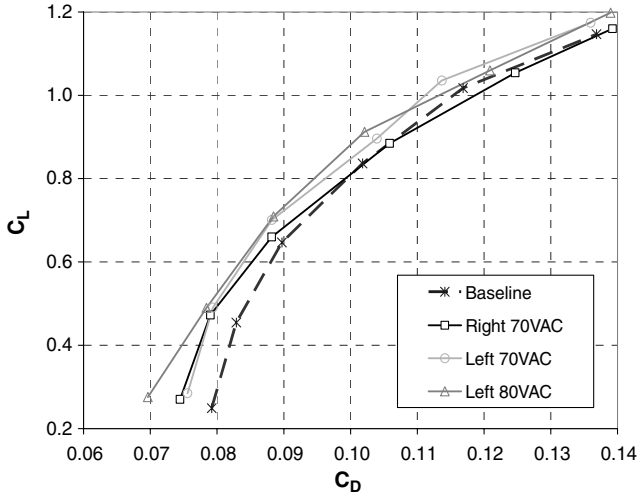

Fig. 14 Baseline and AFC (one wing at a time) lift–drag polar.

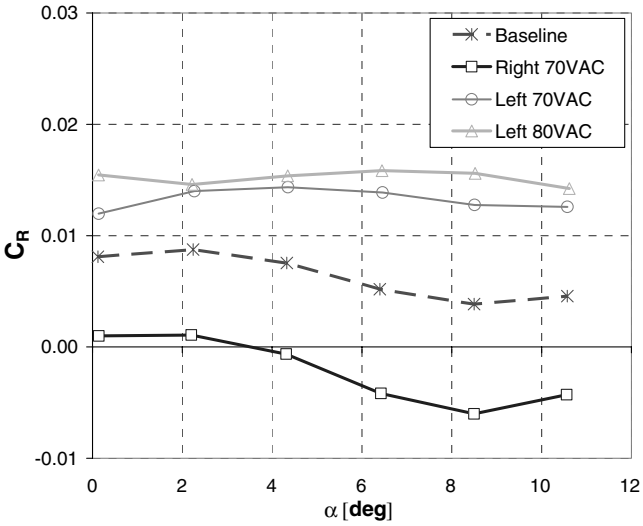

Fig. 15 Rolling moment vs airplane incidence with AFC applied to either the right or left wings ($V = 20$ m/s).

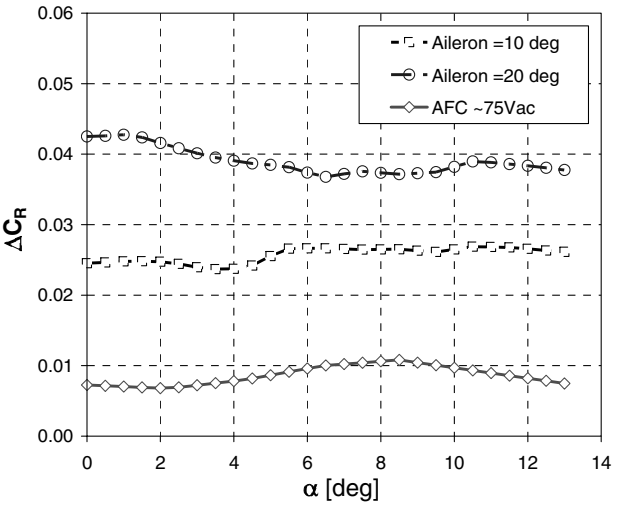

Fig. 17 A comparison of the rolling moment, induced by conventional aileron deflections of 10 and 20 deg, to activation of the one-wing AFC at 70–80 VAC (average of two wings) at $V = 20$ m/s.

drag reduction of about 0.03 in the 2-D Glauert airfoil equivalence, in good agreement with the 2-D airfoil data shown in Figs. 7a and 7b.

Figure 15 shows the airplane rolling moment due to activation of either of the wing actuators at a tunnel speed of 20 m/s and 70–80 VAC. The baseline rolling moment is not exactly zero, because no effort was invested in trimming the plane in the tunnel before additional testing, due to time constraints. A rolling moment alternation, due to actuation close to ± 0.01 with respect to the baseline, can be noted over the entire incidence range. The proportionality of the resulting roll moments due to activation of the control input (i.e., the excitation voltage) is a main concern. Indeed, the 2-D Glauert airfoil tests showed proportional roll moments after the application of the roughness strip upstream of the actuators location (Fig. 6). A similar roughness strip with grit no. 60 was placed on the Glauert sections of the airplane wing (at 40%c) before testing, and the roughness strip was left intact for the flight tests.

The data shown in Fig. 16 indicate a gradual rolling moment alternation due to increasing the voltage provided to the right wing actuators. A threshold of about 40 VAC for the initial response of the rolling moment could be identified, in line with the data of Fig. 6, after the application of the roughness strip to the wing. The response is close to being linear, a highly desirable outcome from the control point of view. Subsequent to identifying the threshold of about 40 VAC for the initial response to actuation, the same threshold level was used for setting the offset on the R/C to the control voltage supplied during the flight tests.

The data shown in Fig. 17 present the rolling moment control authority due to 10 and 20 deg aileron deflections, when compared with activation of the AFC on one wing (the data shown are averaged between two wings, AFC-operated at 70–80 VAC, with the baseline C_R removed). These data were directly measured by the tunnel balance. An average rolling moment of 0.008–0.009 can be noted over the entire tested incidence range. This is comparable with an aileron deflection of 3–4 deg, according to the 10 deg aileron deflection data, or about a third of the control authority. It is noted that the conventional ailerons start to lose effectiveness between 10 and 20 deg.

Figure 18 presents an estimation of the expected airplane maximum roll rates based on the data of Fig. 17. The roll rates were computed using a steady roll rate equation with a damping roll coefficient C_{l_p} of 0.53. Note that the data for 25 m/s are an extrapolation made on lower speed data. It can be seen that a factor of about three between the expected roll rates, based on the deflection of 10 deg ailerons versus the activation of the AFC actuators at about 70 VAC, is expected at a

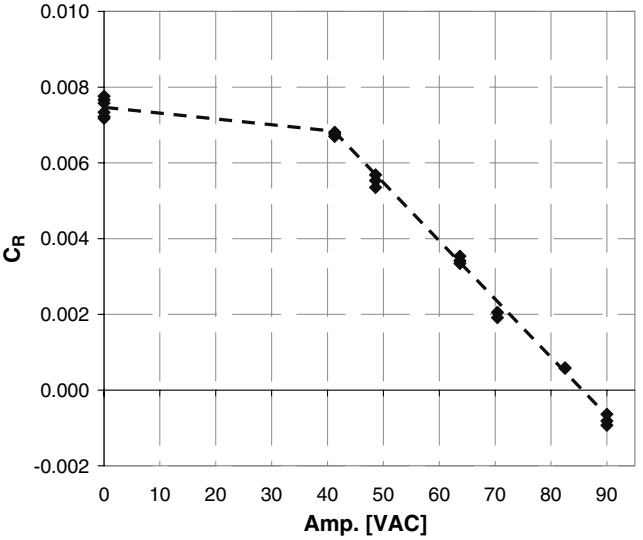

Fig. 16 Airplane rolling moment vs AFC voltage applied to the right wing ($\alpha = 2$ deg, $V = 20$ m/s). Baseline uncontrolled data are for amp = 0 (amplitude increasing).

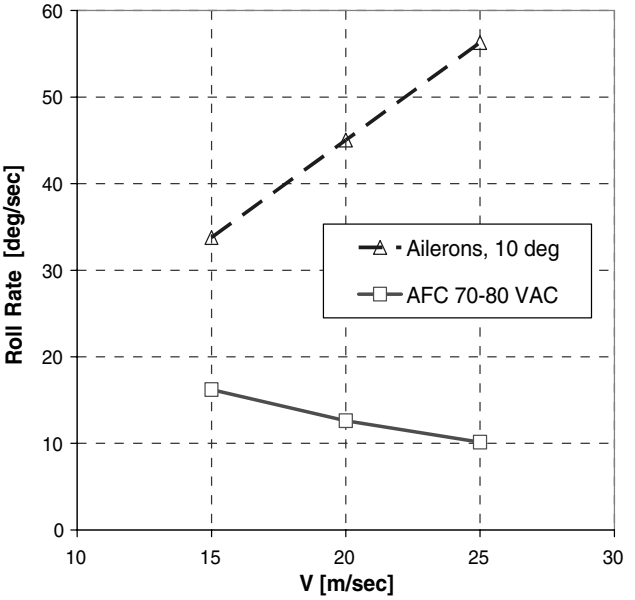

Fig. 18 A comparison between the expected roll rates of 10 deg aileron deflection and AFC-induced roll (using 70–80 VAC) at $V = 15$–25 m/s flight speed, extracted from tunnel data.

flight speed of 20 m/s. Those rates will be compared with the flight-test data near the end of the paper. Also note the highly desirable induced trend of increasing the control authority of the AFC-induced roll rates as the flight speed decreases, whereas the conventional ailerons lose effectiveness. This is because the fluidic excitation level was held fixed while the flight speed decreased, increasing the excitation momentum coefficient and the control authority.

E. Flight Tests

Following the IAI LSWT tests, three flight tests were conducted, each lasting between 10 and 15 min. Figure 19 shows the airplane ready for takeoff at the airfield. The airplane behaved as expected, with no surprises. Sufficient thrust was available, and sufficient control authority in all axes was reported by the experienced pilot. Static stability was not an issue. According to the flight-test data, the stall speed was below 14 m/s. Flight tests were initiated with a conventionally controlled airplane configuration. At a safe altitude of several hundred feet, the flight control was switched to AFC ailerons and, for about five minutes during the first flight, the airplane was roll-controlled using only the AFC ailerons. Figure 20 shows the roll command and the resulting roll angles from the flight-test data, acquired at a 5 Hz sampling rate and transmitted to the ground station. From $t = 1020$ s, and for about five minutes (three minutes are shown here), the data indicate a regular satisfactory flight path while the roll was active-flow controlled. The indicated airspeed for this segment of the flight was between 15 and 25 m/s. Good tracking of the roll angle to the roll command can be identified. The pilot reported no special events but noted "a milder roll response by about a factor of three for a similar stick deflection," although unaware of the specific wind-tunnel test results.

During the second flight test, several controlled maneuvers (doublets) were performed, and the flight terminated with an AFC landing. This was, to the best of our knowledge, one of a handful of instances worldwide when AFC was flight-demonstrated, and it was certainly the first AFC landing.

F. Simulation of Active-Flow-Control-Induced Roll Motion

As a first step in developing a flight-path controller using AFC-induced moments, we have performed several controlled roll maneuvers during the flight-test campaign and attempted to simulate the resulting roll motions for conventional and AFC-induced maneuvers. This was done using a 3-DOF linearized model, using only the flight data (indicated airspeed and stick deflection: roll command) and the wind-tunnel data as inputs to the model. The simulated and measured roll angles are compared next. In total, two conventional maneuvers and three AFC maneuvers were flown and simulated.

The lateral dynamics of the drone were modeled using the 3-DOF linearized equations of motion, implemented on MATLAB® and Simulink. The Simulink model is shown in Fig. 21. It is based on the linearized form of the 3-DOF lateral equations of motion (roll, yaw, and sideslip). The equations follow [19]:

$$qsb\left(C_{l_\beta}\beta + C_{l_r}\frac{b}{2V}\dot{\psi} + C_{l_p}\frac{b}{2V}\dot{\phi} + C_R\right) = I_x\ddot{\phi} \qquad (1)$$

Fig. 19 The airplane ready to be flight tested at the airfield.

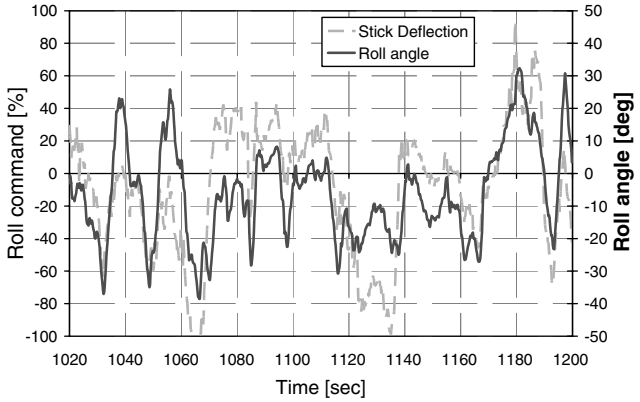

Fig. 20 Flight-test data showing the roll command (left-side ordinate) and roll angle (right-side ordinate) vs time, with roll control induced only via AFC, applied to either the right or left wings using the stick deflection.

$$qsb\left(C_{n_\beta}\beta + C_{n_r}\frac{b}{2V}\dot{\psi} + C_{n_p}\frac{b}{2V}\dot{\phi} + C_n\right) = I_z\ddot{\psi} \qquad (2)$$

$$C_{y_\beta}\beta + C_L\phi = \frac{mV}{qs}(\dot{\beta} + \dot{\psi}) \qquad (3)$$

where C_l is a function of either the aileron deflection angle δ_a when controlled conventionally or the input voltage to the actuators when AFC was applied.

The moments of inertia about the X and Z axis, I_x and I_z, respectively, were estimated by considering the airplane's components as flat plates, rods, and point masses with known geometry and mass locations. The I_x was estimated as 1.5 kg · m^2 and I_z as 2.7 kg · m^2. The stability derivatives C_{l_r} and C_{n_p} were traditionally estimated as $\frac{C_L}{4}$ and $\frac{-C_L}{8}$, respectively, where C_L was calculated assuming straight equilibrium flight and considering the measured indicated air speed from the flight-test data. The remaining stability derivatives were estimated from wind-tunnel tests and actual flight-test data. This was done by fitting the roll angle and roll rate of the model to the flight-test data, in the least-squares sense, and allowing a ±20% deviation from the estimated values from the wind-tunnel data. Finally, these were estimated as (for both control modes)

$$C_{y_\beta} = -0.58; \qquad C_{n_\beta} = 0.09; \qquad C_{l_p} = -0.5$$
$$C_{l_\beta} = -0.14; \qquad C_{n_r} = -0.09$$

The flight data were recorded at a sampling rate of 5 Hz. The roll angle and roll rate of change were extracted from the flight-test data in segments of 7 to 15 s during pilot controlled doublet maneuvers (i.e., sudden roll left, roll right, and back to level flight). The stick deflection was also recorded and converted to either aileron deflection or to AFC actuator voltage, depending on the flight control mode: conventional or AFC roll, respectively. Also, the appropriate model parameters, corresponding to aileron or AFC roll, were used, as extracted from the full-scale-drone wind-tunnel tests. The initial conditions for the roll angle and roll rate were their recorded values at each maneuver's start time. The initial yaw and sideslip angles and rates were assumed as zero. The rudder deflection was not taken into account, as it was not recorded during the flights. Figure 22a compares the actual roll angle and the predicted roll angle in the conventional flight control mode. Figure 22b presents the comparison for the AFC flight mode. As observed from Figs. 22a and 22b, satisfactory agreement was found between the model and flight-test data for both the conventional and the AFC flight modes. A quantification of the rms difference between the flight-test data and the model during the doublet maneuvers shows 11.9 (corresponding to Fig. 22a) and 16.2 deg for the two conventional roll maneuvers and 5.5 (corresponding to Fig. 22b), 10.9, and 13.2 deg for the AFC roll maneuvers.

The mismatch between the two data sets may be partly attributed to the linearized model used, in addition to all the assumptions listed. The lateral equations of motion previously presented in Sec. II.F were

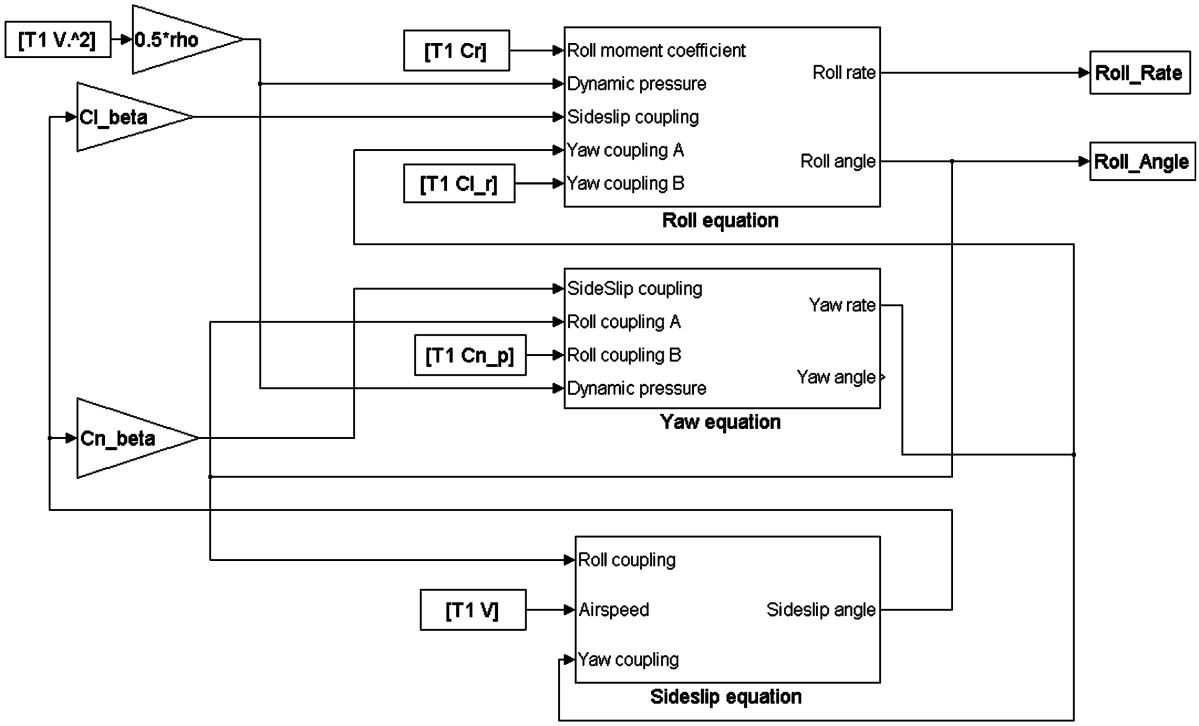

Fig. 21 The 3-DOF Simulink model, described by Eqs. (1–3)

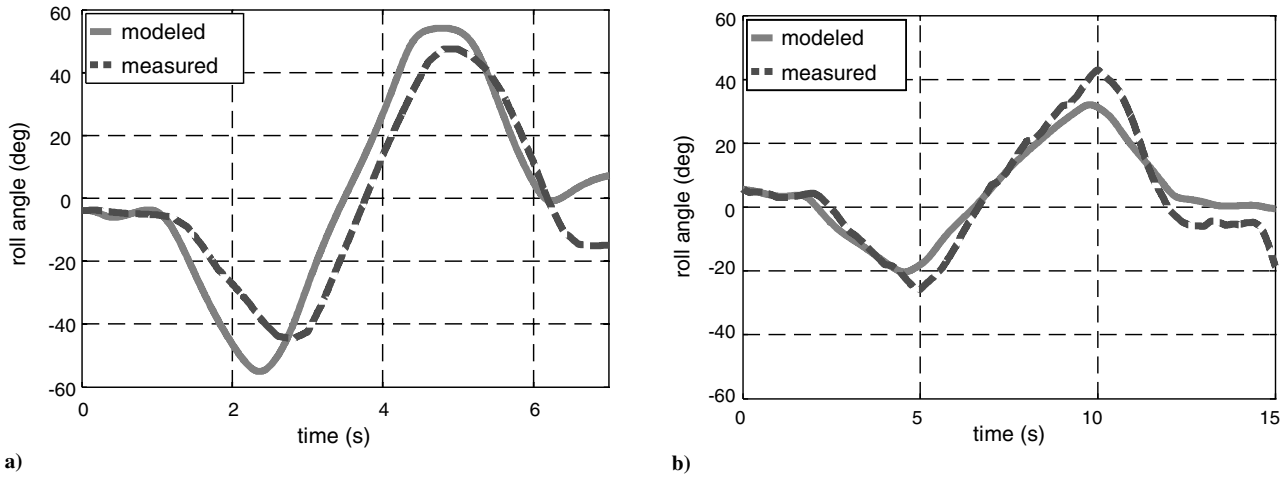

Fig. 22 Actual and computed roll angle a) in conventional flight mode and b) in AFC flight mode: measured data (dashed line) and model (solid line). Note the difference in the total time of each maneuver.

derived assuming small disturbances around straight, level flight at a constant velocity. However, the flight speed, as recorded during the flights, changed significantly during the doublet maneuvers. Furthermore, the roll angles were in the order of ± 30 deg, not quite a small disturbance, as assumed by the linearization. The lack of rudder input to the model was detrimental as well. However, the pilot reported of no requirement to use the rudder during the AFC maneuvers, probably due to the drag reduction accompanying the lift increment, enabling coordinated roll. Also, the low sampling rate of 5 Hz reduced the accuracy of the model. Atmospheric effects, such as winds, were not modeled. Given the indicated limitations, the overall reasonable agreement is almost surprising. Moreover, and most important, the lack of a consistent difference between the models with regard to the two control modes indicates the suitability of existing control models to simulate AFC flight, at least around the roll axis.

III. Conclusions

An intensive design, development, and test program, which took a fundamental AFC concept from laboratory experiments to flight tests, is reported. The purpose of the study was to demonstrate AFC technology in flight and, specifically, to create roll motion without moving control surfaces. The chosen method was to manage the massive flow separation at the aft upper region of a modified Glauert-type airfoil. By installing an array of piezofluidic actuators slightly upstream of the baseline separation region of each wing, it was demonstrated that significant, gradual lift and drag alternations are attainable. A flight actuation system and its electric drive system were developed and lab tested. A small electric airplane was modified to include two segments of the Glauert airfoil, on the midspan section of each wing and extending 25% of the total span each. Operation of the actuators on one wing increased the lift and generated a gradual rolling moment, proportional to the applied voltage, as commanded by the stick deflection. Full-scale wind-tunnel tests, validating the 2-D wind-tunnel test results, were followed by three successful flight tests. They included first-time exclusive roll control via AFC and the first-time landing with the AFC-induced roll motion. A linear 3-DOF flight simulation was performed for estimating the roll motion for conventionally controlled and for AFC flight maneuvers. The good agreement for

both flight modes indicates that conventional controllers using wind-tunnel static data are sufficient, at least for the roll axis.

Acknowledgments

We would like to acknowledge the superb technical and engineering support of M. Goldberg, S. Pasteur, and M. Vassermann of Tel-Aviv University and S. Tsach, S. Meir, and D. Tchetchik of Israel Aerospace Industries (IAI). The collaboration with our IAI colleagues, S. Bauminger, R. Guedj, S. Chester, and A. Abershitz is gratefully acknowledged.

References

[1] Betz, A., "A Method for the Direct Determination of Wing-Section Drag," NACA TM 337, 1925.

[2] Seifert, A., Darabi, A., and Wygnanski, I., "Delay of Airfoil Stall by Periodic Excitation," *Journal of Aircraft*, Vol. 33, No. 4, 1996, pp. 691–698.
doi:10.2514/3.47003

[3] Prandtl, L., Uber Flussigkeits Bewegung bei sehr Kleiner Reibung, *Internationaler 3 Kongreß von Mathematik*, Teubner, Heidelberg, Germany, 1904, pp. 484–491; also "Motion of Fluids with Very Little Viscosity," NACA TM 452, March 1928 (English translation).

[4] Lachmann, G. V., *Boundary-Layer and Flow Control*, Vols. 1–2, Pergamon, Oxford, 1961.

[5] Oster, D., and Wygnanski, I., "The Forced Mixing Layer Between Parallel Streams," *Journal of Fluid Mechanics*, Vol. 123, No. -1, Oct 1982, pp. 91–130.
doi:10.1017/S0022112082002973

[6] Seifert, A., and Pack, L. G., "Oscillatory Control of Separation at High Reynolds Numbers," *AIAA Journal*, Vol. 37, No. 9, 1999, pp. 1062–1071.
doi:10.2514/2.834; also AIAA Paper 98-0214, 1998.
doi:10.2514/2.834

[7] Collis, S. S., Joslin, R. D., Seifert, A., and Theofilis, V., "Issues in Active Flow Control: Theory, Simulation and Experiment," *Progress in Aerospace Sciences*, Vol. 40, No. 4–5, May–July 2004, pp. 237–289.
doi:10.1016/j.paerosci.2004.06.001; also AIAA Paper 2002-3277, 2002.
doi:10.1016/j.paerosci.2004.06.001

[8] Yom-Tov, Y., Dabush, E., Belson, R., and Seifert, A., "Roll Control of an MAV Using Active Flow Control," *Proceedings of the 43rd Israeli Aerospace Meeting* [CD-ROM], Technion, Haifa, Israel, Feb. 2003.

[9] Timor, I., Ben-Hamou, E., Guy, Y., and Seifert, A., "Maneuvering Aspects and 3D Effects of Active Airfoil Flow Control," *Flow, Turbulence and Combustion*, Vol. 78, Nos. 3–4, 2007, pp. 429–443.
doi:10.1007/s10494-006-9065-z; also AIAA Paper 2004-2614, 2004.
doi:10.1007/s10494-006-9065-z

[10] Yom-Tov, Y., and Seifert, A., "Multiple Actuators Flow Control over a Glauert-Type Airfoil at Low Reynolds Numbers," AIAA Paper 2005-5389, June 2005.

[11] Ben-Hamou, E., Arad, E., and Seifert, A., "Air-Jet Actuators and Their Use for Flow Control," *Flow, Turbulence and Combustion* " Vol. 78, Nos. 3–4, 2007, pp. 365–382.
doi:10.1007/s10494-007-9070-x; also "Generic Transport Aft-Body Drag Reduction Using Active Flow Control," AIAA Paper 2004-2509.
doi:10.1007/s10494-007-9070-x

[12] Seifert, A., Stalnov, O., Sperber, D., Arwatz, G., Palei, V., David, S., Dayan, I., and Fono, I., "Heavy Trucks Drag Reduction by Active Flow Control," AIAA Paper 2008-0743, Jan. 2008.

[13] Glauert, M. B., "The Design of Suction Aerofoils with a Very Large CL-Range," Aeronautical Research Council, TR 2111, London, Nov. 1945.

[14] Glauert, M. B., Walker, W. S., Raymer, W. G., and Gregory, N., "Wind-Tunnel Tests on a Thick Suction Aerofoil with a Single Slot," Aeronautical Research Council TR 2646, London, Oct. 1948.

[15] Seifert, A., and Pack, L. G., "Active Control of Separated Flow on a Wall-Mounted Hump at High Reynolds Numbers," *AIAA Journal*, Vol. 40, No. 7, July 2002, pp. 1363–1372.
doi:10.2514/2.1796; also AIAA Paper 99-3430, 1999.
doi:10.2514/2.1796

[16] Arwatz, G., Fono, I., and Seifert, A., "Suction and Oscillatory Blowing Actuator Modeling and Validation," *AIAA Journal*, Vol. 46, No. 5, 2008, pp. 1107–1117.
doi:10.2514/1.30468

[17] Yehoshua, T., and Seifert, A., "Boundary Condition Effects on the Evolution of a Train of Vortex Pairs in Still Air," *Aeronautical Journal*, Vol. 110, No. 1109, Jan. 2006, pp. 397–417.

[18] Seifert, A., Eliahu, S., Greenblatt, D., and Wygnanski, I., "Use of Piezoelectric Actuators for Airfoil Separation Control (TN)," *AIAA Journal*, Vol. 36, No. 8, 1998, pp. 1535–1537.
doi:10.2514/2.549

[19] Perkins, C. D., and Hage, R. E., "Lateral Dynamics," *Airplane Performance Stability and Control*, Wiley, New York, 1949, pp. 419–474.